*Article*

# Effect of Potassium Doping on the Structural and Catalytic Properties of Co/MnOₓ Catalyst in the Steam Reforming of Ethanol

Magdalena Greluk [1,*], Marek Rotko [1], Grzegorz Słowik [1], Sylwia Turczyniak-Surdacka [2], Gabriela Grzybek [3] and Katarzyna Tyszczuk-Rotko [4]

1 Department of Chemical Technology, Faculty of Chemistry, Maria Curie-Sklodowska University in Lublin, Maria Curie-Sklodowska Sq. 3, 20-031 Lublin, Poland
2 Biological and Chemical Research Centre, University of Warsaw, 101 Żwirki i Wigury Street, 20-089 Warsaw, Poland
3 Faculty of Chemistry, Jagiellonian University, Gronostajowa 2, 30-387 Krakow, Poland
4 Department of Analytical Chemistry, Faculty of Chemistry, Maria Curie-Sklodowska University in Lublin, Maria Curie-Sklodowska Sq. 3, 20-031 Lublin, Poland
* Correspondence: magdalena.greluk@mail.umcs.pl; Tel.: +48-81-537-55-14; Fax: +48-81-537-55-65

**Abstract:** The promotional effect of potassium (~1.25 wt%) on a Co/MnOₓ catalyst was studied for samples prepared by the impregnation method in the steam reforming of ethanol (SRE) process at 420 °C for a $H_2O$/EtOH molar ratio of 12/1. The catalysts were characterized using physicochemical methods to study their textural, structural, and redox properties. The XRD studies revealed that, during the treatment of both cobalt-based catalysts under a hydrogen atmosphere at 500 °C, $Co^0$ and MnO phases were formed by the reduction in $Co_3O_4$ and $Mn_2O_3$/$Mn_3O_4$ phases, respectively. Potassium doping significantly improved stability and ability for the C–C bond cleavage of the Co/MnOₓ catalyst. The enhancement of activity (at ~25%) and selectivity to hydrogen (at ca. 10%) and the C1 product, mainly carbon dioxide (at ~20%), of the Co/MnOₓ catalyst upon potassium doping was clarified by the alkali promoter's impact on the reducibility of the cobalt and manganese oxides. The microscopic observations revealed that fibrous carbon deposits are present on the surface of Co/MnOx and KCo/MnOx catalysts after the SRE reaction and their formation is the main reason these catalysts deactivate under SRE conditions. However, carbon accumulation on the surface of the potassium-promoted catalyst was ca. 12% lower after 18 h of SRE reaction compared to the unpromoted sample.

**Keywords:** ethanol steam reforming; hydrogen production; cobalt-based catalysts; manganese oxides; potassium promoter

## 1. Introduction

Hydrogen is considered an ideal energy carrier in fuel cell technology because of its high efficiency. Hydrogen is mainly produced from the steam reforming of fossil fuels, which emit harmful air pollutants into the atmosphere. The steam reforming of ethanol (SRE), $C_2H_5OH + 3H_2O \rightarrow 6H_2 + 2CO_2$, is of interest since it provides a promising method of hydrogen production from renewable resources such as bioethanol, which are easily obtained from biomass. The hydrogen production efficiency first depends on the nature of the catalyst used in the SRE reaction. The preferred catalysts should not be poisoned by carbon monoxide at the reaction temperature, should allow for a fast oxygen transfer and the formation of oxygen vacancy defects, and should contain metals that remain highly active after numerous oxidation-reduction cycles. Cobalt-based catalysts are proposed as more cost-efficient substitutes with a similar C–C bond scission ability in the SRE process to noble-metal-based catalysts. However, their drawback is significant deactivation, which occurs under SRE conditions mainly due to oxidation and sintering of the metallic active

phase, the migration of cobalt ions into the support to form nonreducible mixed-metal cobalt oxides such as aluminates or silicates, and the accumulation of surface carbon species that poison the catalyst by blocking the active surface cobalt sites.

The support materials may strongly influence the catalytic performance of cobalt-based catalysts in the SRE reaction when allowing for the suppression of both cobalt sintering and coke formation [1–6]. Moreover, reducible oxides such as ZnO and $CeO_2$ provide a spillover of oxygen species to the metal particles dispersed on their surfaces, thereby facilitating the oxidation of the carbon deposit [2,3,5,7–11]. However, although manganese oxides possess plenty of active lattice oxygen species that play a role in the efficient elimination of carbon deposition, there are not many reports [1,12–16] on their use as a support for the catalysts of SRE reaction. Both types of manganese oxides with layered and tunnel structures were the subject of this research [12,14,15]. Conventional methods were used to prepare these materials, such as redox precipitation to obtain tunneled structured potassium containing cryptomelane-type manganese dioxide [15], comproportionation reactions of $Mn^{2+}$ and $MnO_4^-$ under alkaline conditions to obtain layer-structure birnessite-type manganese oxide [12,14], or the hydrothermal treatment of layered manganese oxide precursor (birnessite) to obtain tunneled-structure todorokite-type manganese oxide [14,16]. Unfortunately, all these preparative processes of layer- or tunnel-structure manganese oxide have multiple steps and/or are time-consuming. Moreover, all these complex layer- and tunnel-structures of manganese oxide, during hydrogen pretreatment at elevated temperatures, are reduced to lower valence states, an effect that generally gives rise to strong structural and surface changes. The decomposition of the manganese oxides phase into a stable lower valent during the reduction can lead to the collapse of the tunnel structure. For example, Gac et al. [15] indicated that a reduction in the cryptomelane-type manganese oxide led to the development of large, cube-like MnO particles and the disappearance of its tunnel structure. As the activation of the SRE catalysts with hydrogen at elevated temperatures leads to a reduction in the manganese oxides to lower oxidation states with the concomitant evolution of oxygen and complete structural rearrangement, Greluk et al. [16] proposed a simple precipitation method for the preparation of a mixture of chemically simple and inexpensive manganese oxides, $Mn_2O_3$ and $Mn_3O_4$, as a support for the SRE catalyst.

A limitation of the coke deposition might be also achieved by the addition of alkali promoters [16–19], which can significantly change both the structure and surface of the catalyst. The key role of alkali metal additives is dependent on the nature of the catalytic material, e.g., the type and crystallite size of the active phase, the phase composition and the morphology of the support. Moreover, because of the high reactivity and volatility of alkalis, the high-temperature pretreatment of SRE catalysts and the interaction of numerous reagents of the SRE process can result in undesired processes such as alkali surface redistribution, a solid-state reaction with the active phase/support, their agglomeration, or even alkali promoters' desorption, affecting the resulting performance of the catalyst. Therefore, the promotional effect of alkali must be elucidated individually for each catalytic system [17,20].

To our knowledge, no studies were conducted to investigate the impact of the potassium promoter on manganese-oxide-supported, cobalt-based catalysts in the SRE reaction. Therefore, this work aimed to determine the role that potassium promotion plays in the performance of the $Co/MnO_x$ catalyst during the SRE process. The chemical and physical properties of catalysts were characterized by BET, XRF, XRD, TPR, SEM, TEM and XPS methods.

## 2. Materials and Methods

### 2.1. Materials

The materials used in the preparation of samples: manganese(II) acetate tetrahydrate (≥97.0%, Sigma-Aldrich, Darmstadt, Germany), cobalt(II) nitrate hexahydrate (≥98.0%,

Sigma-Aldrich), potassium nitrate ($\geq$99.0%, Merck, Darmstadt, Germany) and ammonium carbonate (100%, Avantor, Gliwice, Poland) were used without further purification.
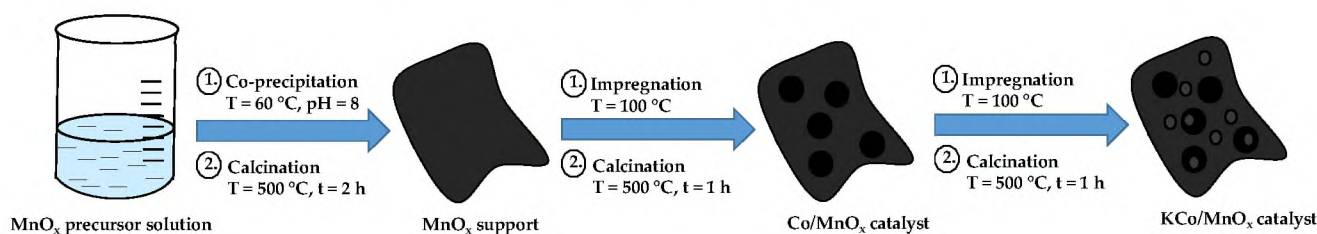
## 2.2. Preparation of Catalysts

The $MnO_x$ support was prepared using the precipitation method with 1 mol/L ammonium carbonate solution as a precipitant from the precursor of manganese acetate. Ammonium carbonate solution was added dropwise to manganese acetate solution with vigorous stirring until a pH of 8 was maintained at 40 °C. The resulting precipitate was aged at 60 °C for 2 h. The suspension was filtered and then washed several times with deionized water until reaching a pH of 7. The precipitate was then dried at 110 °C and calcined at 500 °C in air.

The $Co/MnO_x$ catalysts were prepared using the impregnation method by mixing cobalt nitrate solution and $MnO_x$ support to achieve 10 wt% cobalt loading. The sample was dried at 110 °C and calcined at 500 °C in air.

The $KCo/MnO_x$ catalysts were prepared using the impregnation method by mixing potassium nitrate solution and $Co/MnO_x$ sample to achieve 2 wt% potassium loading. The sample was dried at 110 °C and calcined at 500 °C in air.

A schematic drawing of the preparations of $MnO_x$ support and $Co/MnO_x$ and KCo/MnOx catalysts is presented in Figure 1.



**Figure 1.** A schematic drawing of the preparations of $MnO_x$ support and $Co/MnO_x$ and $KCo/MnO_x$ catalysts.

## 2.3. Catalysts Characterization

Details about the physicochemical characterization of materials can be found in our previous work [16]. The metal loading of catalysts was determined by the X-ray fluorescence method, using an Axios mAX (PANalytical, Malvern, UK) fluorescence spectrometer. The BET surface area, pore volume, and pore diameter of the samples were measured by ASAP 2405N (Micromeritics, Norcross, GA, USA) instrument, using nitrogen adsorption/desorption isotherms collected at −196 °C. The X-ray powder diffraction (XRD) patterns were obtained with an Empyrean X-ray (PANalytical, Malvern, UK) diffractometer. Temperature-programmed reduction (TPR) studies were carried out with an AutoChem II 2920 (Micromeritics, Norcross, GA, USA) analyzer. The high-resolution transmission electron microscopy (HRTEM) images of catalysts were obtained with an electron transmission microscope Titan G2 60–300 kV (FEI Company, Hillsboro, OR, USA). X-ray photoelectron spectroscopy (XPS) studies were performed in a Kratos Axis Supra Spectrometer (Kratos Analytical, Manchester, UK) equipped with a monochromatized Al source.

## 2.4. SRE Experimental Tests

The catalyst activity test was carried out in a quartz tube reactor (inner diameter: 10 mm) using a Microactivity Reference unit (PID Eng & Tech., Alcobendas, Spain). The reactor was filled with a catalyst sample diluted with quartz. A total of 100 mg of catalyst sample was reduced with hydrogen at 500 °C for 1 h. After this reduction, the performance was evaluated at atmospheric pressure, a temperature of 420 °C and a $H_2O/EtOH$ molar ratio of 12/1, with a total flow rate equal to 100 mL $min^{-1}$. The reaction substrates and products were analyzed by online gas chromatographs (Bruker 430-GC and Bruker 450-GC, (Bruker, Billerica, MA, USA) equipped with thermal conductivity detectors (TCD).

The conversion of ethanol, conversions of ethanol into individual carbon-containing products and the selectivity of hydrogen formation were calculated based on the previously reported equations [16].

## 3. Results and Discussion

### 3.1. The Effect of Potassium Doping on the Catalysts' Physicochemical Properties

The results of BET analysis, quantitative analysis (analyzed by XRF method), and values of average crystallite size (analyzed by XRD and TEM methods) of $Co/MnO_x$ and $KCo/MnO_x$ catalysts are summarized in Table 1. The desired loading of cobalt (10 wt%) was obtained with good accuracy. However, the potassium promoter content is less than the intended loading of 2 wt%. The $Co/MnO_x$ catalyst exhibits a low surface area, which decreases by more than 50% following re-calcination after the addition of a potassium promoter. Because the low surface area of support does not facilitate the dispersion of metal particles, both $Co/MnO_x$ and $KCo/MnO_x$ catalysts exhibit a large $Co^0$ particle size (see also Supplementary Materials, Figure S1). The slightly larger size of $Co^0$ particles for $KCo/MnO_x$ catalysts results from the agglomeration of the initially formed cobalt species crystallites of the Co/MnOx catalyst during its second calcination, after impregnation with potassium salt [18]. STEM-EDS maps of samples, after their reduction with hydrogen at 500° (Figures 2 and 3), reveal a comparatively homogenous cobalt dispersion on the $MnO_x$ support of both catalysts, as well as potassium accumulation on both $MnO_x$ and $Co^0$ particles for the K-doped sample.
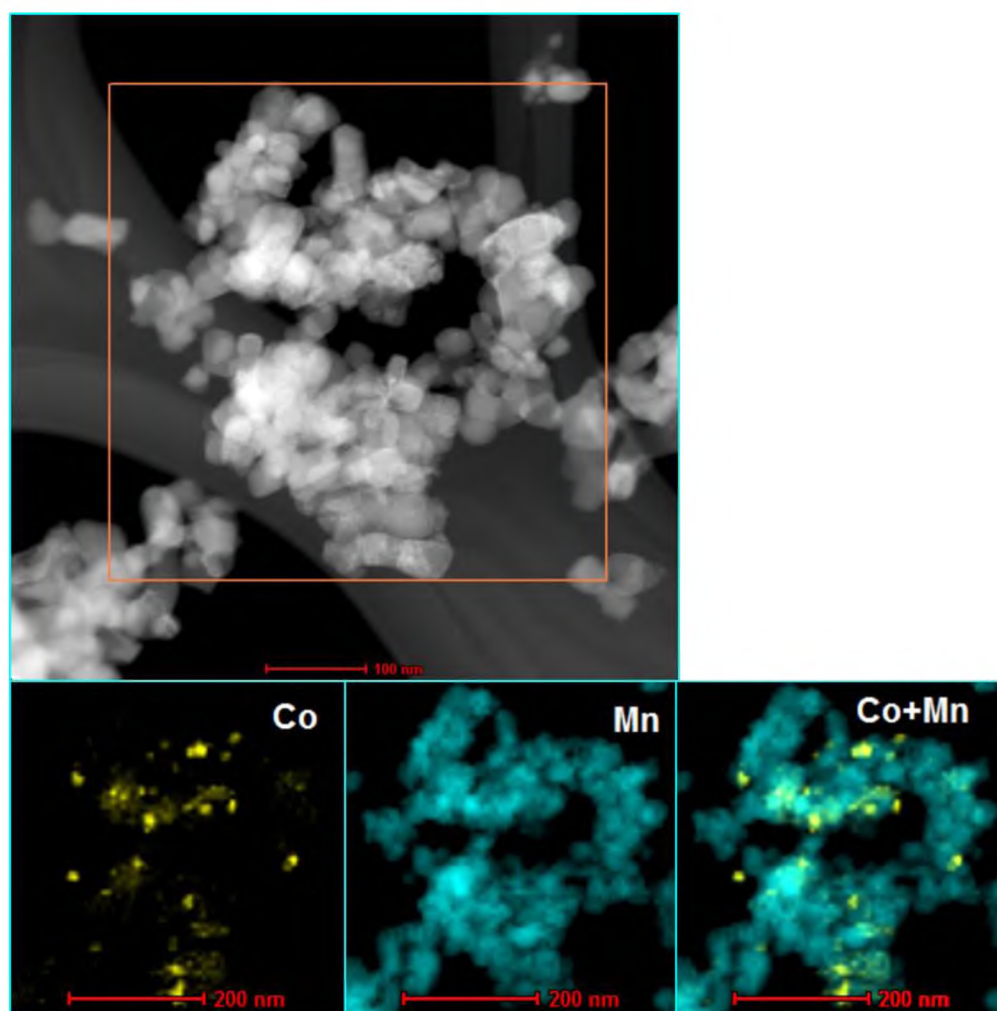


**Figure 2.** STEM-EDS analysis of $Co/MnO_x$ catalyst after their reduction with hydrogen at 500 °C.

**Table 1.** Physicochemical parameters for $Co/MnO_x$ and $KCo/MnO_x$ catalysts.

| Parameter | | $Co/MnO_x$ | $KCo/MnO_x$ |
|---|---|---|---|
| Metal content (wt%) | | 9.7 | 9.7 |
| Potassium content (wt%) | | - | 1.25 |
| BET surface area ($m^2/g$) | | 11.2 | 5.8 |
| $Co^0$ crystallite size (nm) [1] | By XRD | 14 | 23 |
| | By TEM | 21 | 26 |
| $H_2$ consumption | Theoretical ($mmol/g_{Co}$) | 2.18 | 2.19 |
| | Experimental (mmol/g) | 5.21 | 7.23 |

[1] $Co^0$ denoted Co particle size for a catalyst reduced at 500 °C.
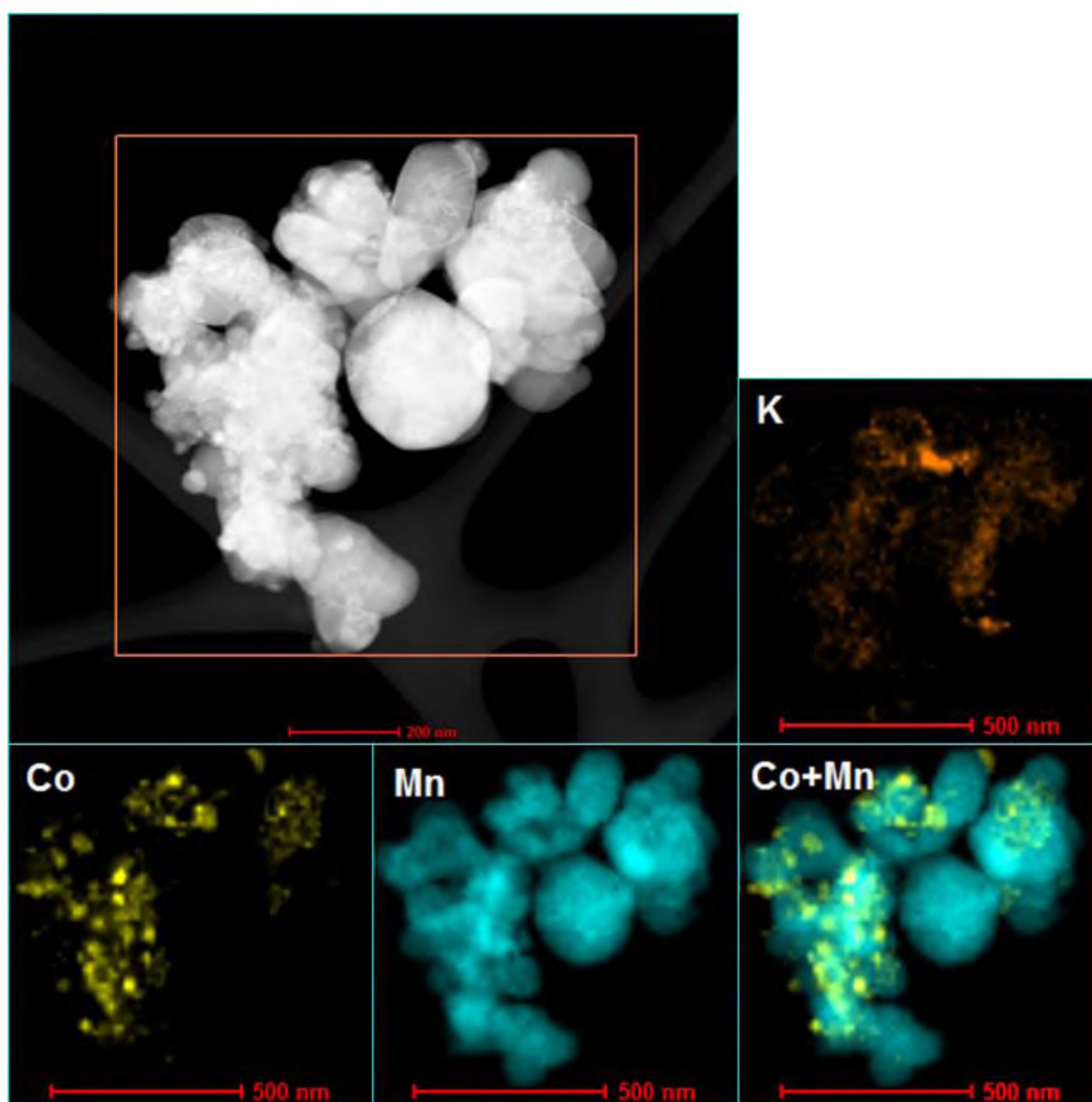


**Figure 3.** STEM-EDS analysis of $KCo/MnO_x$ catalyst after their reduction with hydrogen at 500 °C.

Figure 4A,B shows the XRD patterns of the calcined $Co/MnO_x$ and $KCo/MnO_x$ catalysts, which reveal that both $Co/MnO_x$ and $KCo/MnO_x$ samples contain a mixture of tetragonal $Mn_3O_4$ (JCPDS file no. 04-005-9818) and cubic $Mn_2O_3$ phases (JCPDS file no. 00-001-1127). However, in the case of both catalysts, the major species is $Mn_2O_3$. Diffraction peaks observed at diffraction angles (2θ) of 24.0°, 33.1°, 38.6°, 45.3°, 49.5°,

$55.2°$, $60.9°$ and $66.0°$ can be assigned to the (211), (222), (400), (332), (431), (400), (611) and (622) crystalline planes of the cubic $Mn_2O_3$ crystal. Similarly, prominent diffraction peaks appeared at $2\theta$ of $28.0°$, $31.4°$, $32.2°$, $36.1°$, $44.8°$, $58.8°$, $60.0°$, which can be assigned to the (112), (200), (103), (211), (220), (321) and (224) crystalline planes of the tetragonal $Mn_3O_4$ phase. Moreover, because the main reflection for $Mn_3O_4$ at $2\theta = 33.1°$ is nearly identical to the main reflection of $Co_3O_4$ (JCPDS file no. 04-002-0644) at $2\theta = 36.1°$, the possibility that these both reflections overlap should not be excluded. However, the XRD pattern of both catalysts mainly diffracts at angles that can attributed to the phases of support due to its much higher content compared to the $Co_3O_4$ active phase. Upon the reduction in both cobalt-based catalysts for 2 h at 500 °C, the XRD peaks corresponding to the cubic-phase $Mn_2O_3$ and tetragonal-phase $Mn_3O_4$ disappeared completely, and new reflections that appeared at $34.9°$, $40.4°$, $58.5°$, $70.0$ and $73.6°$ are mainly present, which can be assigned to the (111), (200), (220), (311) and (222) planes of the cubic structure of MnO (JCPDS file no. 00-075-1090) (Figure 4C,D). In addition to the predominant diffraction peaks derived from the MnO support, weaker diffraction lines at $2\theta = 43.7°$ and $51.2°$, corresponding to the reflection planes of the $Co^0$ phase, are visible [16,21–28]. Moreover, the absence of any potassium phase for the $KCo/MnO_x$ catalyst in the XRD patterns may result from several factors, namely its considerably low amount and/or amorphous form and/or high dispersion over the catalyst surface [16,29]. Unfortunately, due to the low potassium-promoter content, there is a problem with the understanding of its role, since it is difficult to characterize this on the catalytic surface [29].
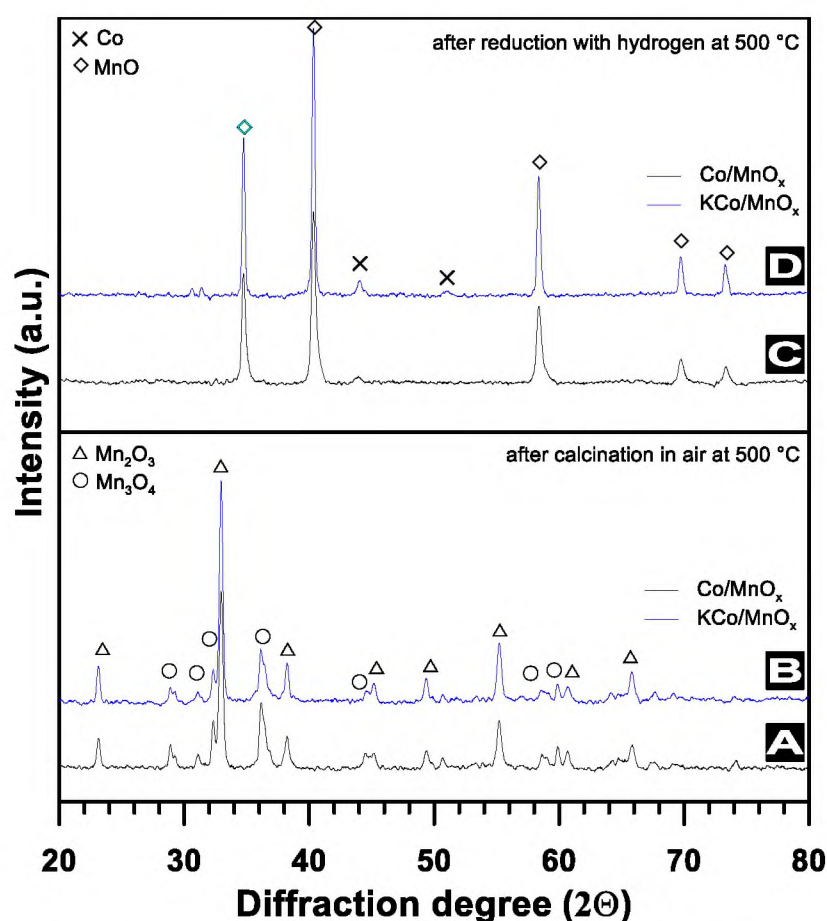


**Figure 4.** XRD patterns of $Co/MnO_x$ and $KCo/MnO_x$ catalysts after their calcination in-air at 500 °C (**A,B**) and after their reduction with hydrogen at 500 °C (**C,D**).

Detailed HRTEM measurements (Figures 5 and 6) were taken for both cobalt-based catalysts after their reduction at 500 °C, and the results are in good agreement with the

XRD findings. Well-crystallized $Co^0$ and MnO phases are identified for both $Co/MnO_x$ (Figure 5) and $KCo/MnO_x$ (Figure 6) catalysts. For both catalysts, HRTEM images reveal lattice fringes with an interplanar spacing of 0.205, 0.222 and 0.225 nm, which may be ascribed to the (111) plane of $Co^0$, (200) and (111) planes of MnO, respectively. Moreover, for the $Co/MnO_x$ sample, lattice fringes with an interplanar spacing of 0.157 nm, which can be ascribed to the (220) planes of MnO, are also observed. The planes of both samples were also identified by the spots on the corresponding FFT pattern.
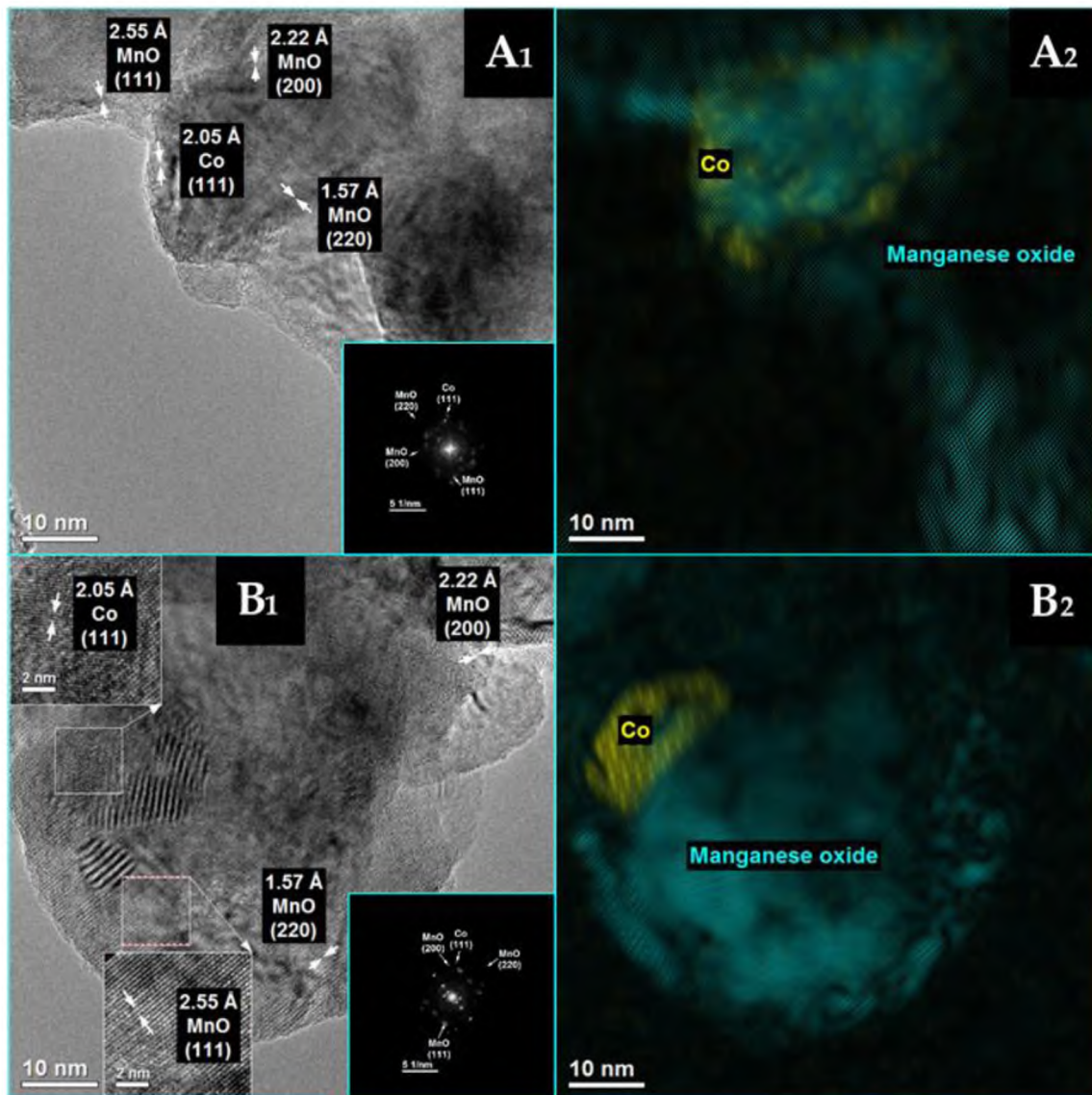


**Figure 5.** HRTEM images from different points (**A₁**,**B₁**) of $Co/MnO_x$ catalyst after reduction with hydrogen at 500 °C with the complementary phase identification ((**A₂**,**B₂**), $Co^0$—yellow; MnO—turquoise) and the corresponding fast Fourier transform (FFT) patterns in the turquoise squares as the inset of (**A₁**,**B₁**). Arrows represent distance between the two the two lattice planes. Magnified view of the selected areas was enclosed in the dashed square to show diffraction fringes and their respective interplanar distances.
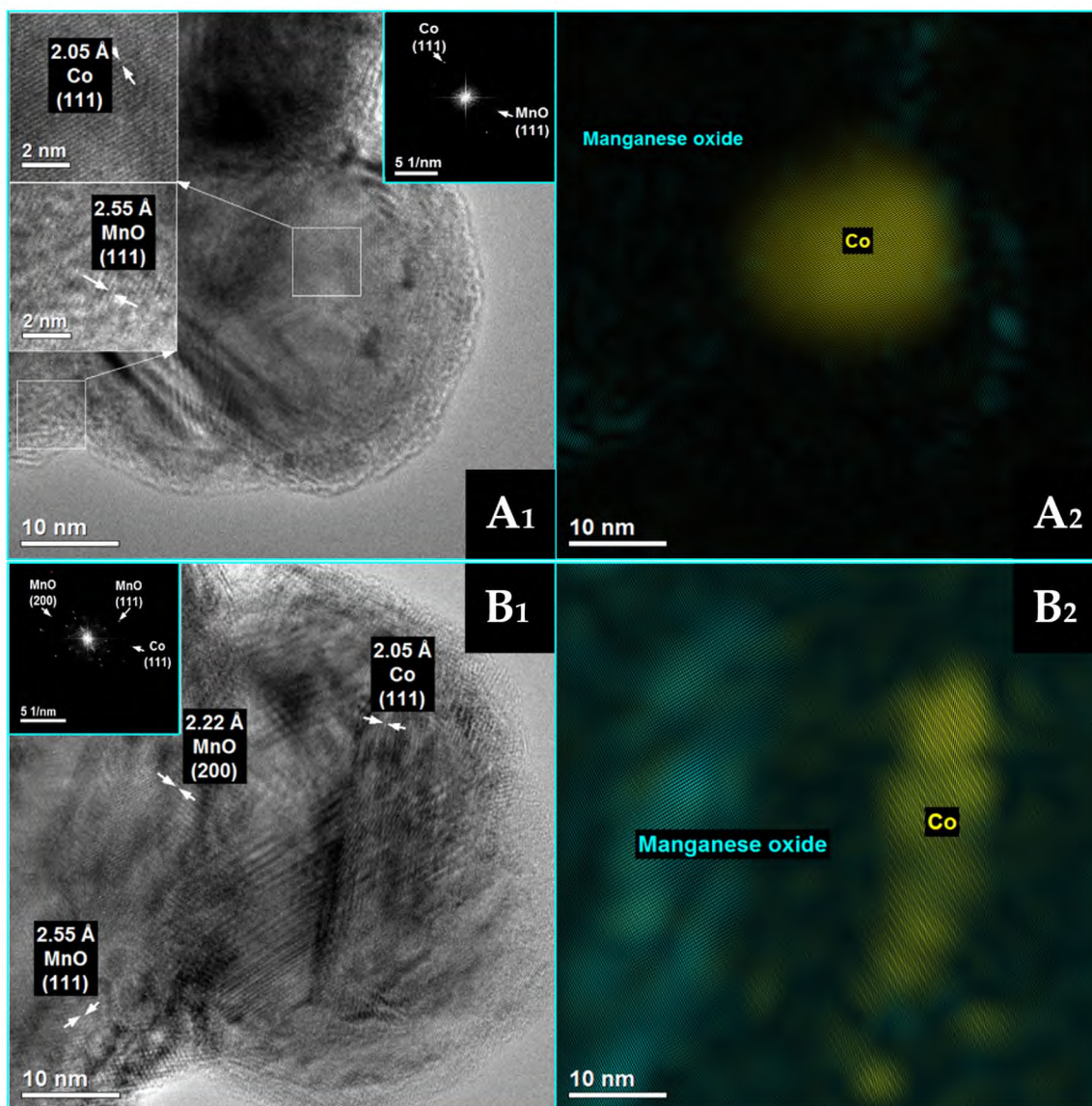
**Figure 6.** HRTEM images from different points (**A₁**,**B₁**) of KCo/MnOₓ catalyst after its reduction with hydrogen at 500 °C with the complementary phase identification ((**A₂**,**B₂**), Co⁰—yellow; MnO— turquoise) and the corresponding fast Fourier transform (FFT) patterns in the turquoise squares as the inset of (**A₁**,**B₁**). Arrows represent distance between the two the two lattice planes. Magnified view of the selected areas was enclosed in the dashed square to show diffraction fringes and their respective interplanar distances. Obtained from the HRTEM image in (**A**).

The reducibility of the MnOₓ support, Co/MnOₓ and KCo/MnOₓ catalysts, was also studied by the H₂-TPR method, and the results are displayed in Figure 7. According to the literature [16,30–33], bare MnOₓ exhibits a low-temperature peak at 220–330 °C, which can be assigned to the reduction from Mn₂O₃ to Mn₃O₄ and high temperature at ca. 330–520 °C, corresponding to the transformation of Mn₃O₄ to MnO. Based on the study of the literature [34,35], due to two reduction steps, the H₂-TPR profile of Co₃O₄ has a low-temperature peak below 300 °C, assigned to the reduction from Co₃O₄ to CoO, and a high-temperature peak between 300 and 700 °C, corresponding to the further reduction from CoO to Co⁰. This means that the reduction peaks in manganese oxides overlapped with those of cobalt oxides and could not be distinguished. The H₂-TPR profile of the Co/MnOₓ catalyst has two regions of hydrogen consumption: a low-temperature region at 220–310 °C and a high-temperature region at 310–750 °C, which could correspond to the reduction from Mn₂O₃ to Mn₃O₄ and Co₃O₄ to CoO, and the reduction from Mn₃O₄ to MnO

and CoO to $Co^0$, respectively. Moreover, the broad peak observed in the high-temperature region (above 500 °C) could be a result of the synergetic interactions between Mn and Co species [36]. A reduction in the K-containing sample leads to a lower temperature compared to a reduction in $Co/MnO_x$ material. In addition, two reduction peaks were observed that could be ascribed to the stepwise reduction in manganese and cobalt oxides. Moreover, a small shoulder below 260 °C is related to the presence of surface-active species with different Mn–O bond strengths [16,37]. The KCo/MnOx sample (Table 1) exhibits high hydrogen consumption, which may result from the reduction in nitrates stored on the catalyst's surface, facilitated by the presence of potassium [16]. It can be supposed that the nitrate reducibility is increased by the presence of cobalt and hydrogen, which is dissociated upon the $Co^0$ particles' spilling onto the nitrate, reducing their quantity [38].
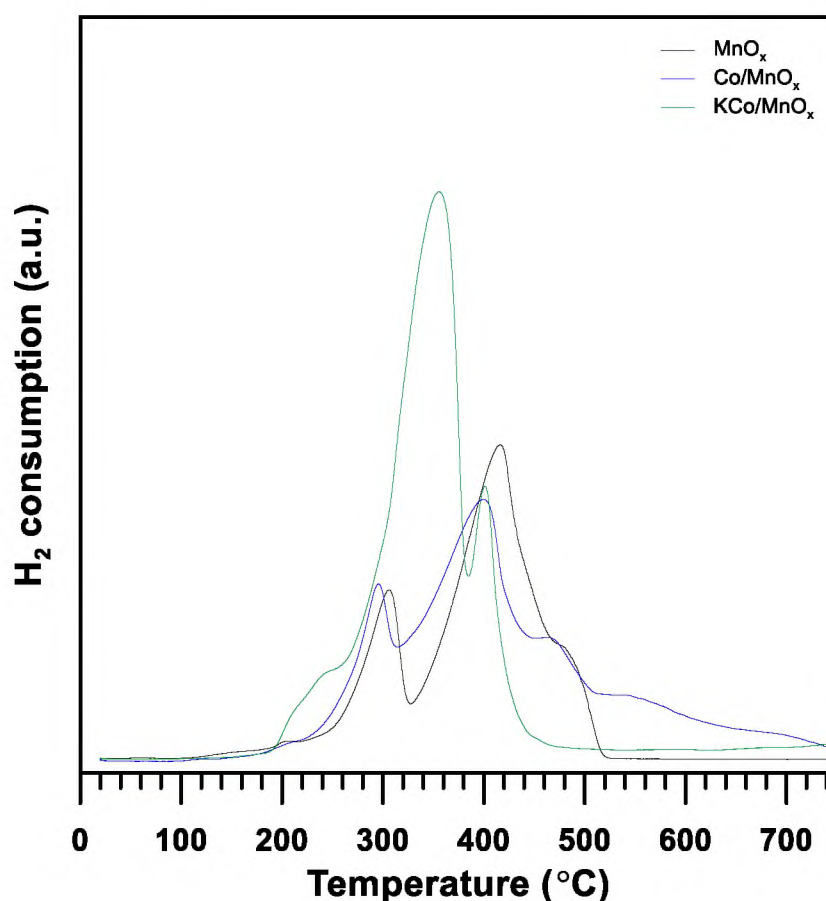


**Figure 7.** $H_2$-TPR profiles of $MnO_x$ support and $Co/MnO_x$ and $KCo/MnO_x$ catalysts.

### 3.2. The Effect of Potassium Doping on the Performance of the Catalysts in the Ethanol Steam Reforming Reaction

The effect of potassium doping on the cobalt-based catalyst in the SRE process was determined by ethanol conversion (Figure 8) and selectivity to products (Figure 9) at the temperature of 420 °C for a $H_2O/EtOH$ molar ratio of 12/1. The initial complete conversion of ethanol decreases after 18 h of the SRE process to ca. 40 and 70% over $Co/MnO_x$ and $KCo/MnO_x$ catalysts, respectively. At the beginning of the SRE reaction, the $KCo/MnO_x$ catalyst exhibits high selectivity to hydrogen and carbon dioxide. In contrast, hydrogen and carbon monoxide are mainly produced in the presence of the $Co/MnO_x$ sample, which suggests an increase in activity in water gas shift (WGS, Reaction (1)) reactions in the presence of a potassium-doped catalyst:

$$CO + H_2O \leftrightarrow CO_2 + H_2 \qquad (1)$$
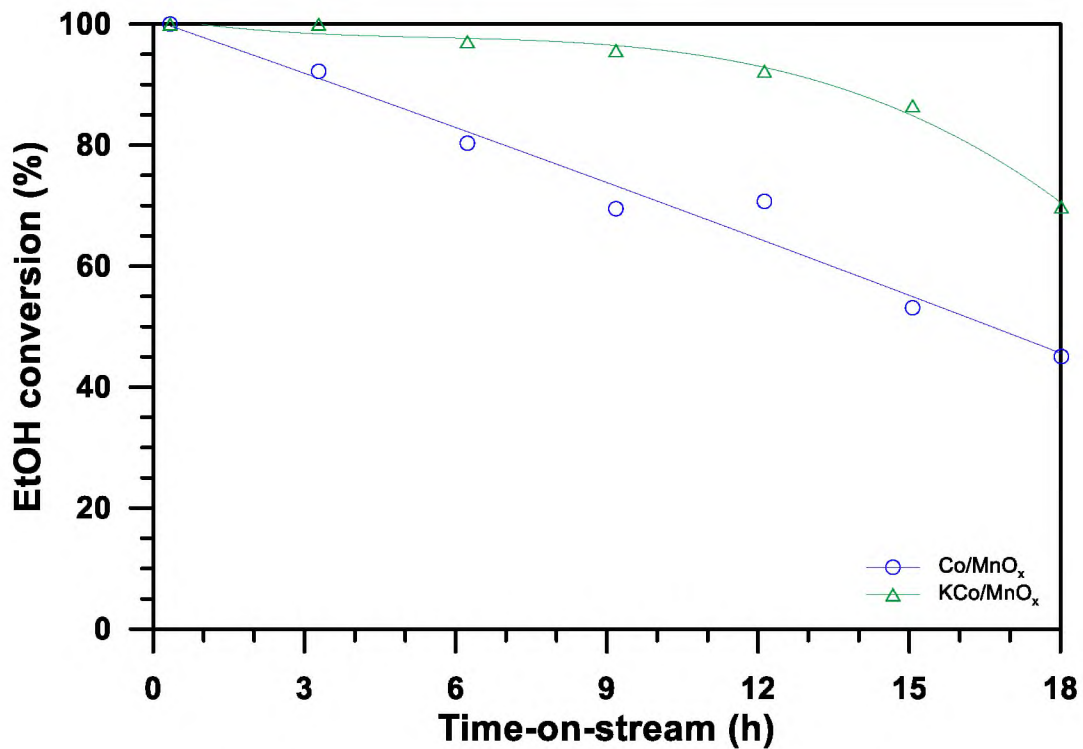
**Figure 8.** The ethanol conversion over $Co/MnO_x$ and $KCo/MnO_x$ catalysts after 18 h of the SRE process at 420 °C for an $H_2O/EtOH$ molar ratio of 12/1.
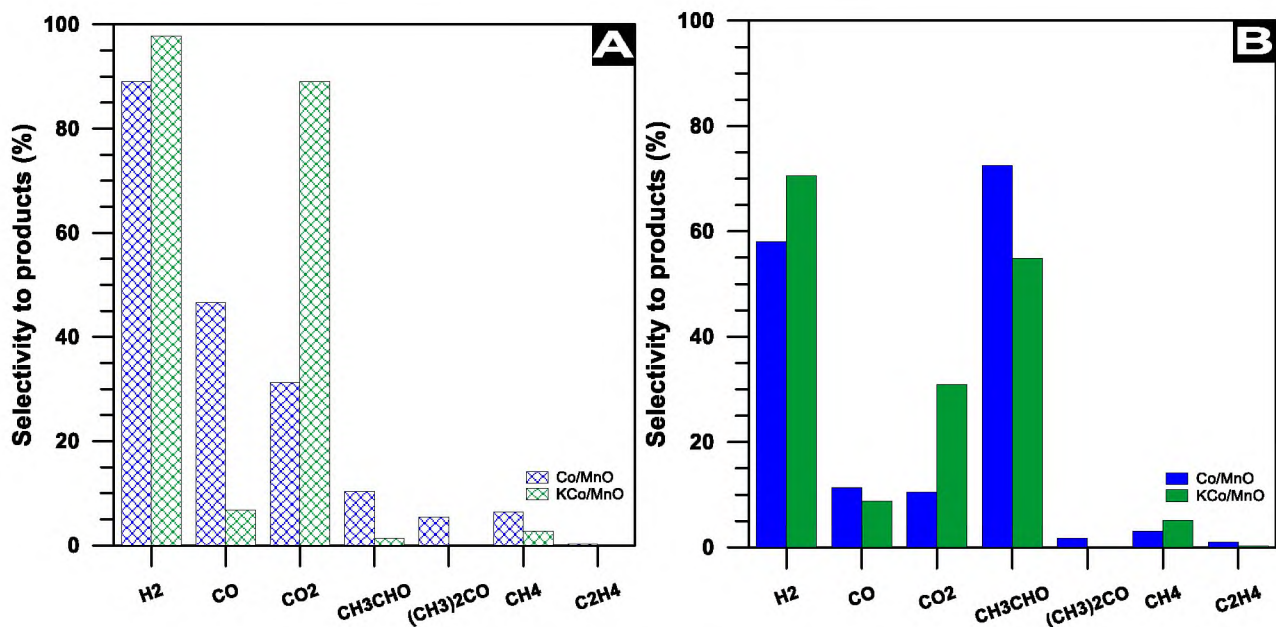


**Figure 9.** The selectivity to products at the beginning (**A**) and after 18 h (**B**) of the SRE process at 420 °C for a $H_2O/EtOH$ molar ratio of 12/1 over $Co/MnO_x$ and $Kco/MnO_x$ catalysts.

Furthermore, the C2 and C3 products, i.e., acetaldehyde, ethylene and acetone, are present among the by-products of a $Co/MnO_x$ sample from the beginning of the SRE reaction, which indicates the poor ability of this catalyst in terms of the C–C bond cleavage. The addition of potassium allows for restrictions to the production of these products and, initially, only small amounts of acetaldehyde are formed over the $KCo/MnO_x$ sample. However, the amount of this product drastically increases with the increase in time-on-stream over both cobalt-based catalysts. After 18 h of the SRE process, selectivity to

acetaldehyde is ca. 70 and 55% for $Co/MnO_x$ and $KCo/MnO_x$ catalysts, respectively. Next to hydrogen, it is the second product that is mainly produced in the presence of these catalysts during the SRE process. This indicates that the ability of both samples in the C–C bond scission decreases with the increase in time-on-stream because of the deactivation of cobalt active sites on the catalysts' surface under SRE conditions. However, the lower selectivity to the C2 and C3 products and higher selectivity to the C1 products suggests that more cobalt-active sites remained available on the surface of the $KCo/MnO_x$ catalyst to break the C–C bond.

### 3.3. The Effect of Potassium Doping on Prevention of the Cobalt-Based Catalyst Deactivation under SRE Conditions

The microscopic (Figures 10 and 11) observations revealed that fibrous carbon deposits are present on the surface of $Co/MnO_x$ and $Kco/MnO_x$ catalysts. The cobalt nanocrystals are almost completely detached from the $MnO_x$ support by carbon deposits, and they are either confined to the fibres or located at the tip of the carbon filaments, being totally or partially surrounded by a carbon shell.
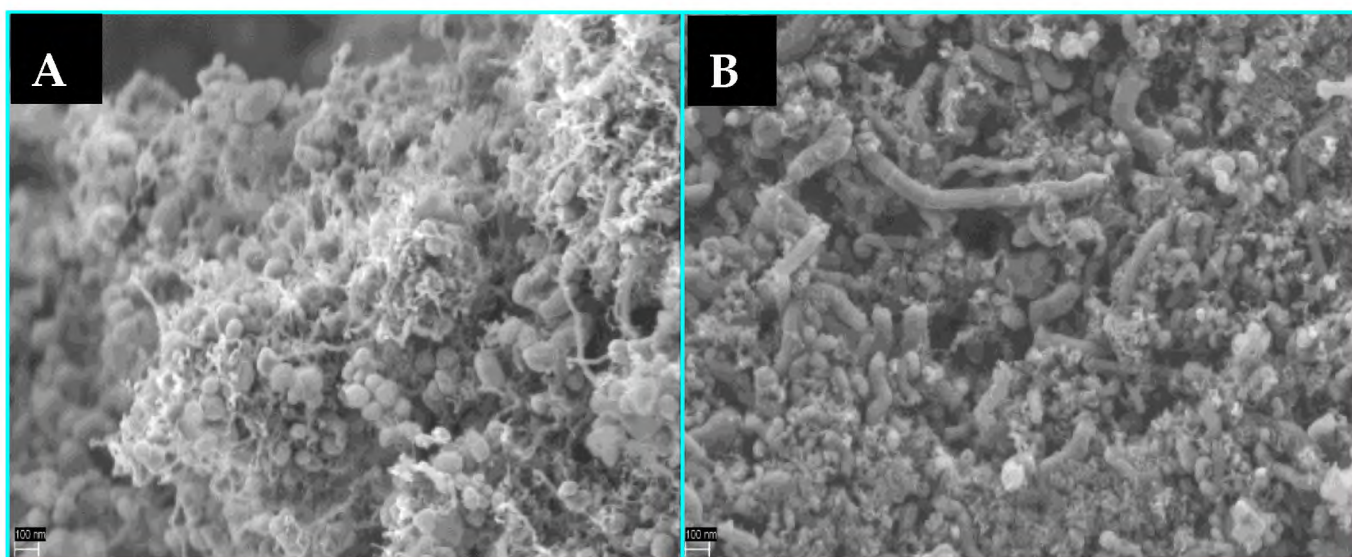


**Figure 10.** SEM images of $Co/MnO_x$ (**A**) and $KCo/MnO_x$ (**B**) catalyst after 18 h of SRE reaction at 420 °C for $H_2O/EtOH$ molar ratio of 12/1.

Based on the HRTEM images and the corresponding phase identification obtained using the FFT method (Figure 11), two forms of cobalt-active phase were identified in the case of the spent $Co/MnO_x$ catalyst, namely $Co^0$ and $CoO$. However, the $Co^0$ form of the cobalt-active phase was detected for the spent $KCo/MnO_x$ catalyst. Moreover, support for the $Co/MnO_x$ sample was identified as including two forms, $MnO$ and $Mn_2O_3$, where only the $MnO$ phase was detected for the support of the spent KCo/MnOx catalyst.

Figure 12 shows the amount of carbon deposits that were formed on the surface of the $Co/MnO_x$ and $KCo/MnO_x$ catalysts as a function of time. The rate of carbon formation significantly decreased in the presence of a potassium promoter on the surface of a cobalt-based catalyst, indicating that its addition can inhibit carbon deposition and/or promote gasification [16]. Potassium species probably migrated and covered the surface of the $Co^0$ particles, which favoured the adsorption-dissociation of the $H_2O$ molecule, and therefore increased the direct oxidation of the carbonaceous species [39].
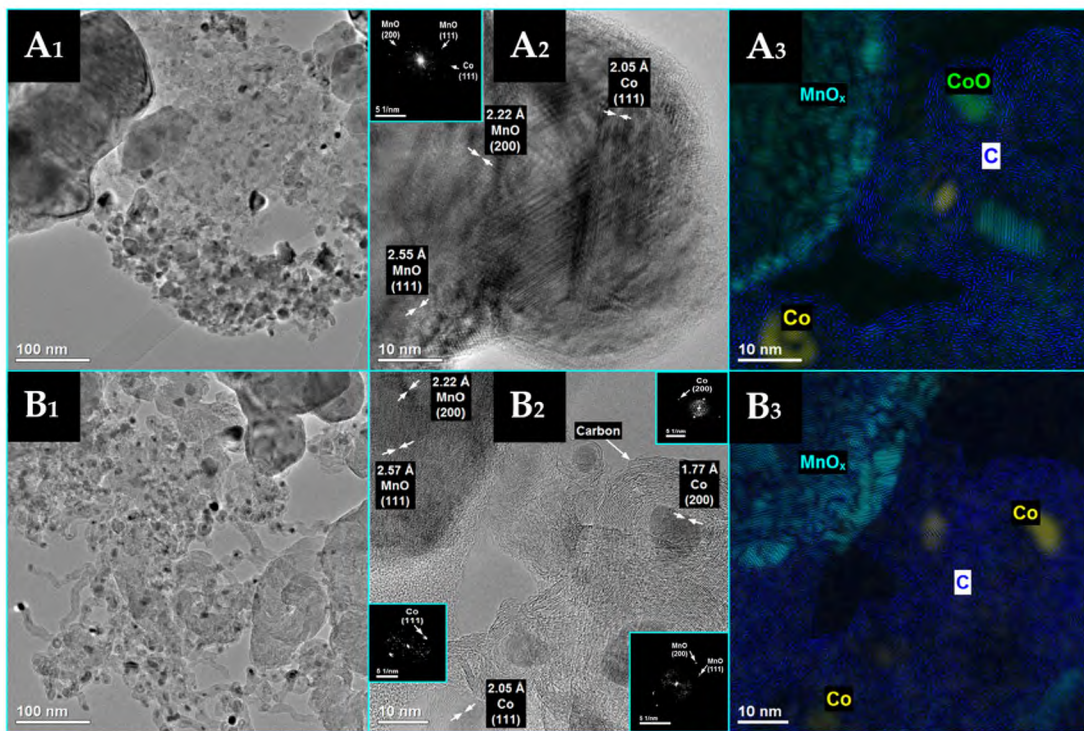
**Figure 11.** Microscopic analysis of Co/MnO$_x$ (**A**) and KCo/MnO$_x$ (**B**) catalyst after 18 h of SRE reaction at 420 °C for H$_2$O/EtOH molar ratio of 12/1. TEM images (**A$_1$,B$_1$**), HRTEM images (**A$_2$,B$_2$**) and the corresponding phase identification (**A$_3$,B$_3$**), Co$^0$—yellow; CoO—green, MnO—turquoise, C—blue).
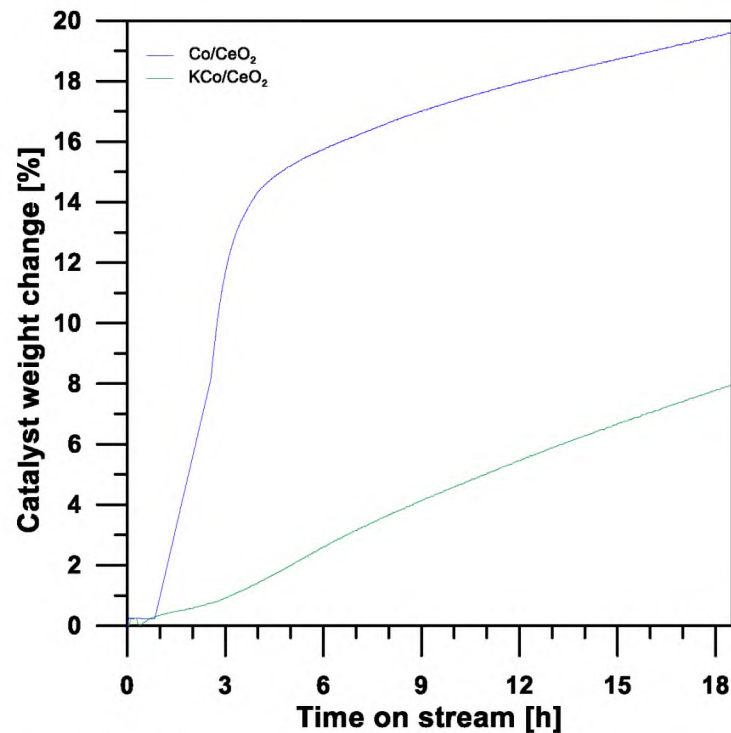


**Figure 12.** Changes in Co/MnOx and KCo/MnOx catalysts' weight during 18 h of SRE reaction at 420 °C for H$_2$O/EtOH molar ratio of 12/1.

The survey spectra of spent cobalt-based catalysts (H$_2$O/ethanol = 12/1, 420 °C) show the major signals originating from C, O and Mn elements, and minor signals originating

from Co. The atomic surface coverage by carbon deposits was estimated at around 81.5 at.% for Co/MnOx and 91 at.% for KCo/MnO$_x$ catalysts. Most of the carbon exists in graphitic-like compounds, as confirmed by the asymmetric C 1s peak shape (284.5 eV, not shown here). The high carbon coverage of the surface leads us to expect that most crystallites of the active phase and support were occluded in carbon; therefore, their oxidation state remained unchanged even upon exposure to air (Figure 13). The Co 2p3/2 spectrum can be resolved into components, which are attributed to the Co–Co (778.4 eV) and Co–O bonding (780.4 eV), respectively [40,41]. A higher concentration of metallic cobalt species can be observed for the potassium-promoted catalyst, suggesting that this promotor plays a very important role in the reduction in the active phase. For the manganese oxidation state, the literature data [41] suggest that MnO and Mn$_2$O$_3$ phases are present. The relative concentration of Mn(II)/(Mn(II) + Mn(III)) in both samples is very similar, in the range of 51%. The interpretation of the results obtained for bare manganese support requires a comparison of both the spectrum recorded for the as-calcined sample and after ESR reaction. This is important, as bare support was rather inactive in the ESR [18], whereas the survey spectrum suggests almost 55 at.% coverage of the surface by carbon-containing species. This result seems less surprising when one notes that the atomic contribution of adventitious carbon species on the surface of the calcined sample is equal to 39 at.%. The calculation of the relative concentration of Mn(II) in the overall Mn 2p3/2 spectrum suggests a lower concentration of these species (43%) as compared to the results obtained for cobalt-based catalysts.
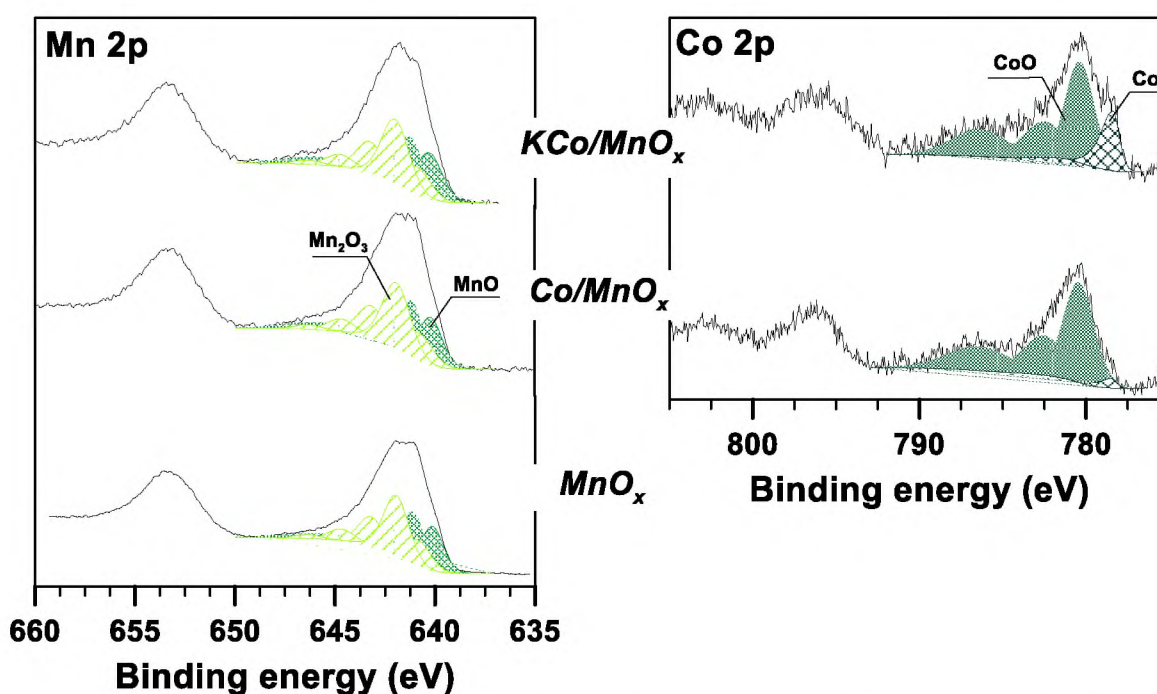


**Figure 13.** High-resolution XPS spectra of Mn 2p and Co 2p regions collected from the surface of Co/MnO$_x$ and KCo/MnO$_x$ catalysts after 18 h of SRE reaction at 420 °C for H$_2$O/EtOH molar ratio of 12/1.

## 4. Conclusions

The doping effect of a potassium-promoter on the novel Co/MnO$_x$ catalytic material's performance in the SRE reaction was studied, focusing on the catalyst's ability to resist carbon growth. It is beneficial to consider the significant increase in catalytic stability achieved by the Kco/MnO$_x$ catalyst in comparison with the Co/MnO$_x$ sample, and the distribution of the products over these catalysts under SRE conditions. Compared with the unpromoted Co/MnO$_x$ catalyst, the Kco/MnO$_x$ sample indicated an increase in the

selectivity to two main products of the SRE reaction, i.e., hydrogen (Co/MnO$_x$—ca. 55% and Kco/MnO$_x$—ca. 70%) and carbon dioxide (Co/MnO$_x$—ca. 20% and Kco/MnO$_x$— ca. 40%). In turn, selectivity to C2 products was ca. 20% higher in the presence of an unpromoted Co/MnO$_x$ sample, indicating that more cobalt-active sites remained available on the surface of the KCo/MnO$_x$ catalyst to cleave the C–C bond. Although fibrous carbon was present on the surface of both Co/MnO$_x$ and KCo/MnO$_x$ samples, the carbon accumulation was ca. 12% higher on the surface of unpromoted catalysts after 18 h of SRE reaction. This indicates that potassium species probably migrated and covered the surface of the Co$^0$ particles, which favoured the adsorption–dissociation of the H$_2$O molecule, and therefore increased the direct oxidation of the carbonaceous species. It could be concluded that the crucial effect of potassium dopant is the decrease in carbon accumulation on the catalyst surface and the increase in the number of sites for water adsorption, which improve the catalyst stability. Furthermore, the alkali metal could change the electronic properties of the cobalt species, and hence facilitate the redox ability of active sites both during activation with hydrogen and under SRE conditions. The maintenance of a reduced oxidation state for the catalyst surface during the SRE process is important to ensure an effective C—C bond; thus, the catalytic stability of a potassium cobalt-based catalyst was improved. According to the results of the characterization, the addition of the alkali metal did not influence the cobalt active-phase dispersion, but was not a key parameter improving Co/MnO$_x$ catalysts' activity, selectivity and resistance to deactivation.

**Supplementary Materials:** The following supporting information can be downloaded at: https://www.mdpi.com/article/10.3390/ma16155377/s1, Figure S1: Particle size distribution histograms for (**a**) Co/MnOx and (**b**) KCo/MnOx catalysts reduced at 500 °C.

**Author Contributions:** Conceptualization, M.G.; formal analysis, M.G. and G.G.; funding acquisition, G.G.; investigation, M.G., M.R., G.S., S.T.-S., G.G. and K.T.-R.; methodology, M.G., M.R., G.S., S.T.-S., G.G. and K.T.-R.; supervision, M.G.; writing—original draft, M.G.; visualization, M.G.; writing—review and editing, M.G. All authors have read and agreed to the published version of the manuscript.

**Institutional Review Board Statement:** Not applicable.

**Informed Consent Statement:** Not applicable.

**Conflicts of Interest:** The authors declare no conflict of interest.

# References

1. Sohrabi, S.; Irankhah, A. Synthesis, characterization, and catalytic activity of Ni/CeMnO$_2$ catalysts promoted by copper, cobalt, potassium and iron for ethanol steam reforming. *Int. J. Hydrogen Energy* **2021**, *46*, 12846–12856. [CrossRef]
2. Yu, S.-W.; Huang, H.-H.; Tang, C.-W.; Wang, C.-B. The effect of accessible oxygen over Co$_3$O$_4$-CeO$_2$ catalysts on the steam reforming of ethanol. *Int. J. Hydrogen Energy* **2014**, *39*, 20700–20711. [CrossRef]
3. Liu, Z.; Duchoň, T.; Wang, H.; Peterson, E.W.; Zhou, Y.; Luo, S.; Zhou, Y.; Matolín, V.; Stacchiola, D.J.; Rodriguez, J.A.; et al. Mechanistic insight of ethanol steam reforming over Ni-CeO$_x$(111): The importance of hydroxyl groups for suppressing coke formation. *J. Phys. Chem C* **2015**, *119*, 18248–18256. [CrossRef]
4. Zhu, S.; Liu, L. A comparative DFT study of ethanol steam reforming over Co(1 0 0) and CoO(1 0 0) surfaces: Molecular reaction mechanism. *Comput. Theor. Chem.* **2022**, *1217*, 113926. [CrossRef]
5. Idriss, H. Ethanol reactions over the surfaces of noble metal/cerium oxide catalysts. *Platin. Met. Rev.* **2004**, *48*, 105–115. [CrossRef]
6. Passos, A.R.; Martins, L.; Pulcinelli, S.H.; Santilli, C.V.; Briois, V. Effect of the balance between Co(II) and Co(0) oxidation states on the catalytic activity of cobalt catalysts for Ethanol Steam Reforming. *Catal. Today* **2014**, *229*, 88–94. [CrossRef]
7. Liu, X.; Murata, K.; Inaba, M. Steam Reforming of Bio-Ethanol to Produce Hydrogen over Co/CeO$_2$ Catalysts Derived from Ce$_{1-x}$Co$_x$O$_{2-y}$ Precursors. *Catalysts* **2016**, *6*, 26. [CrossRef]
8. You, W.; Zhang, Q.; Jia, H.; Ta, N.; Sheng, X.; Yang, X.; Wang, Y.; Shen, W.; Goldbach, A. Insights into the state of ceria during ethanol steam reforming over Ir/CeO$_2$. *Catal. Sci. Technol.* **2023**, *13*, 558–572. [CrossRef]
9. Palma, V.; Castaldo, F.; Ruocco, C.; Ciambelli, P.; Iaquaniello, G. Low temperature-ethanol steam reforming over Ni-based catalysts supported on CeO$_2$. *J. Power Technol.* **2015**, *95*, 54–66.

10. Chiou, J.Y.Z.; Wang, W.-Y.; Yang, S.-Y.; Lai, C.-L.; Huang, H.-H.; Wang, C.-B. Ethanol Steam Reforming to Produce Hydrogen Over Co/ZnO and PtCo/ZnO Catalysts. *Catal. Lett.* **2013**, *143*, 501–507. [CrossRef]

11. Yu, N.; Zhang, H.; Davidson, S.D.; Sun, J.; Wang, Y. Effect of ZnO facet on ethanol steam reforming over Co/ZnO. *Catal. Commun.* **2016**, *73*, 93–97. [CrossRef]

12. Da Costa-Serra, J.F.; Chica, A. Catalysts based on Co-Birnessite and Co-Todorokite for the efficient production of hydrogen by ethanol steam reforming. *Int. J. Hydrogen Energy* **2018**, *43*, 16859–16865. [CrossRef]

13. Kwak, B.S.; Lee, G.; Park, S.-M.; Kang, M. Effect of $MnO_x$ in the catalytic stabilization of $Co_2MnO_4$ spinel during the ethanol steam reforming reaction. *Appl. Catal. A Gen.* **2015**, *503*, 165–175. [CrossRef]

14. Fuertes, A.; Da Costa-Serra, J.F.; Chica, A. New catalysts based on Ni-Birnessite and Ni-Todorokite for the efficient production of hydrogen by bioethanol steam reforming. *Energy Procedia* **2012**, *29*, 181–191. [CrossRef]

15. Gac, W.; Greluk, M.; Słowik, G.; Turczyniak-Surdacka, S. Structural and surface changes of cobalt modified manganese oxide during activation and ethanol steam reforming reaction. *Appl. Surf. Sci.* **2018**, *440*, 1047–1062. [CrossRef]

16. Greluk, M.; Rotko, M.; Słowik, M.; Turczyniak-Surdacka, S.; Grzybek, G.; Góra-Marek, K.; Kotarba, A. Effect of Potassium Promoter on the Performance of Nickel-Based Catalysts Supported on MnOx in Steam Reforming of Ethanol. *Catalysts* **2022**, *12*, 600. [CrossRef]

17. Grzybek, G.; Góra-Marek, K.; Tarach, K.; Pyra, K.; Patulski, P.; Greluk, M.; Słowik, G.; Kotarba, A. Tuning the properties of the cobalt-zeolite nanocomposite catalyst by potassium: Switching between dehydration and dehydrogenation of ethanol. *J. Catal.* **2022**, *407*, 364–380. [CrossRef]

18. Grzybek, G.; Greluk, M.; Tarach, K.; Pyra, K.; Słowik, G.; Rotko, M.; Góra-Marek, K. Bioethanol Steam Reforming over Cobalt-Containing USY and ZSM-5 Commercial Zeolite Catalysts. *Front. Mater.* **2020**, *7*, 597528. [CrossRef]

19. Yoo, S.; Park, S.; Song, H.; Kim, D.H. Hydrogen production by the steam reforming of ethanol over K-promoted $Co/Al_2O_3$–CaO xerogel catalysts. *Mol. Catal.* **2020**, *491*, 110980. [CrossRef]

20. Grzybek, G.; Wójcik, S.; Legutko, P.; Gryboś, J.; Indyka, P.; Leszczyński, B.; Kotarba, A.; Sojka, Z. Thermal stability and repartition of potassium promoter between the support and active phase in the $K-Co_{2.6}Zn_{0.4}O_4$ | $\alpha$-$Al_2O_3$ catalyst for $N_2O$ decomposition: Crucial role of activation temperature on catalytic performance. *Appl. Catal. B Environ.* **2017**, *205*, 597–604. [CrossRef]

21. Sengottaiyan, C.; Jayavel, R.; Shrestha, R.G.; Hill, J.P.; Ariga, K.; Shrestha, L.K. Electrochemical Supercapacitance Properties of Reduced Graphene Oxide/$Mn_2O_3$:$Co_3O_4$ Nanocomposite. *J. Inorg. Organomet. Polym.* **2017**, *27*, 576–585. [CrossRef]

22. Sharrouf, M.; Awad, R.; Roumié, M.; Marhaba, S. Structural, Optical and Room Temperature Magnetic Study of Mn2O3 Nanoparticles. *Mater. Sci. Appl.* **2015**, *6*, 850–859.

23. Gnana Sundara Raj, B.; Asiri, A.M.; Wu, J.J.; Anandan, S. Synthesis of $Mn_3O_4$ nanoparticles via chemical precipitation approach for supercapacitor application. *J. Alloys Compd.* **2015**, *636*, 234–240. [CrossRef]

24. Khalaji, A.D.; Soleymanifard, M.; Jarosova, M.; Machek, P. Facile synthesis and characterization of $Mn_3O_4$, $Co_3O_4$, and NiO. *Acta Phys. Pol.* **2002**, *137*, 1043–1045. [CrossRef]

25. Ciura, K.; Grzybek, G.; Wójcik, S.; Indyka, P.; Kotarba, A.; Sojka, S. Optimization of cesium and potassium promoter loading in alkali-doped $Zn_{0.4}Co_{2.6}O_4$ | $Al_2O_3$ catalysts for $N_2O$ abatement. *React. Kinet. Mech. Catal.* **2017**, *121*, 645–655. [CrossRef]

26. Hou, H.; Li, J.; Lan, J.; Chen, F.; Huang, B. Porous walnut-like $Mn_2O_3$ anode derived from the waste graphene production effluent. *J. Porous Mater.* **2022**, *29*, 837–847. [CrossRef]

27. Atique Ullah, A.K.M.; Fazle Kibria, A.K.M.; Akter, M.; Khan, M.N.I.; Tareq, A.R.M.; Firoz, S.H. Oxidative Degradation of Methylene Blue Using $Mn_3O_4$ Nanoparticles. *Water Conserv. Sci. Eng.* **2017**, *1*, 249–256. [CrossRef]

28. Martinez de la Torre, C.; Bennewitz, M.F. Manganese oxide nanoparticle synthesis by thermal decomposition of manganese(II) acetylacetonate. *J. Vis. Exp.* **2020**, *160*, e61572.

29. Grzybek, G.; Greluk, M.; Indyka, P.; Góra-Marek, K.; Legutko, P.; Słowik, G.; Turczyniak-Surdacka, S.; Rotko, M.; Sojka, Z.; Kotarba, A. Cobalt catalyst for steam reforming of ethanol–Insights into the promotional role of potassium. *Int. J. Hydrogen Energy* **2020**, *45*, 22658–22673. [CrossRef]

30. Li, J.; Li, L.; Cheng, W.; Wu, F.; Lu, X.; Li, Z. Controlled synthesis of diverse manganese based catalysts for complete oxidation of toluene and carbon monoxide. *Chem. Eng. J.* **2014**, *22*, 59–67. [CrossRef]

31. Shu, S.; Guo, J.; Li, J.; Fang, N.; Li, J.; Yuan, S. Effect of post-treatment on the selective catalytic reduction of NO with $NH_3$ over $Mn_3O_4$. *Mater. Chem. Phys.* **2019**, *237*, 121845. [CrossRef]

32. Gil, A.; Gandía, L.M.; Korili, S.A. Effect of the temperature of calcination on the catalytic performance of manganese- and samarium-manganese-based oxides in the complete oxidation of acetone. *Appl. Catal. A Gen.* **2004**, *274*, 229–235. [CrossRef]

33. Chen, Z.; Yang, Q.; Li, H.; Li, X.; Wang, L.; Tsang, S.C. $Cr–MnO_x$ mixed-oxide catalysts for selective catalytic reduction of $NO_x$ with $NH_3$ at low temperature. *J. Catal.* **2010**, *276*, 56–65. [CrossRef]

34. Lin, H.-Y.; Chen, Y.-W. The mechanism of reduction of cobalt by hydrogen. *Mater. Chem. Phys.* **2004**, *85*, 171–175. [CrossRef]

35. Darda, S.; Pachatouridou, E.; Lappas, A.; Iliopoulou, E. Effect of preparation method of Co-Ce catalysts on $CH_4$ combustion. *Catalysts* **2019**, *9*, 219. [CrossRef]

36. Zhong, L.; Barreau, M.; Chen, D.; Caps, V.; Haevecker, M.; Teschnerb, D.; Simonne, D.H.; Borfecchia, E.; Baaziz, W.; Šmí, B.; et al. Effect of manganese promotion on the activity and selectivity of cobalt catalysts for CO preferential oxidation. *Appl. Catal. B Environ.* **2021**, *297*, 120397. [CrossRef]

37. Zhang, X.; Yang, Y.; Zhu, Q.; Ma, M.; Jiang, Z.; Liao, X.; He, C. Unraveling the effects of potassium incorporation routes and positions on toluene oxidation over α-$MnO_2$ nanorods: Based on experimental and density functional theory (DFT) studies. *J. Colloid Interface Sci.* **2021**, *598*, 324–338. [CrossRef]

38. Grzona, C.B.; Lick, I.D.; Rodriguez Castellón, E.; Ponzi, M.I.; Ponzi, E.N. Cobalt and $KNO_3$ supported on alumina catalysts for diesel soot combustion. *Mater. Chem. Phys.* **2010**, *123*, 557–562. [CrossRef]

39. Claude, V.; Mahy, J.G.; Lohay, T.; Tilkin, R.G.; Micheli, F.; Lambert, S.D. Sol–gel synthesis of Ni/$Al_2O_3$ catalysts for toluene reforming: Support modification with alkali, alkaline earth or rare-earth dopant (Ca, K, Mg or Ce). *Surf. Interfaces* **2020**, *20*, 100511. [CrossRef]

40. Yildirim, O.A.; Arslan, H.; Sönmezoglu, S. Facile synthesis of cobalt-doped zinc oxide thin films for highly efficient visible light photocatalysts. *Appl. Surf. Sci.* **2016**, *390*, 111–121. [CrossRef]

41. Biesinger, M.C.; Payne, B.P.; Grosvenor, A.P.; Lau, L.V.M.; Gerson, A.R.; Smart, R.S.C. Resolving surface chemical states in XPS analysis of first row transition metals, oxides and hydroxides: Cr, Mn, Fe, Co and Ni. *Appl. Surf. Sci.* **2011**, *257*, 2717–2730. [CrossRef]